Chemical Engineering Journal 434 (2022) 134681

Contents lists available at ScienceDirect

Chemical Engineering Journal

journal homepage: www.elsevier.com/locate/cej

A stochastic DNA walker electrochemiluminescence biosensor based on quenching effect of Pt@CuS on luminol@Au/Ni-Co nanocages for ultrasensitive detection of I27L gene

Wei Gong [a,1], Jia Shu [b,1], Pan Ju [a], Shaoyan Wu [a], Yuzhou Chen [c], Shijia Ding [d], Wei Yang [c,*], Rong Luo [a,*]

[a] Medical Examination Centre, The First Affiliated Hospital of Chongqing Medical University, Chongqing 400016, China
[b] Department of Ophthalmology, The First Affiliated Hospital of Chongqing Medical University, Chongqing 40016, China
[c] Department of Clinical Laboratory, Zhejiang Provincial People's Hospital, People's Hospital of Hangzhou Medical College, Hangzhou 310014, China
[d] Key Laboratory of Clinical Laboratory Diagnostics (Ministry of Education), College of Laboratory Medicine, Chongqing Medical University, Chongqing 400016, China

ARTICLE INFO

Keywords:
Electrochemiluminescence resonance energy transfer
Luminol
Prussian blue analogs
CuS nanospheres
I27L gene

ABSTRACT

The common I27L mutations of the hepatocyte nuclear factor-1α (HNF1A) significantly increase the incidence of maturity-onset diabetes of the young (MODY). Hence, the establishment of an ultrasensitive detection strategy for I27L gene is crucial for the diagnosis and treatment of MODY. Herein, a signal-off electrochemiluminescence resonance energy transfer (ECL-RET) biosensor with effective target-induced stochastic DNA walker amplification was fabricated for I27L detection. In this biosensor, Prussian blue analogues (Ni-Co) nanocages/Au-supported luminol (luminol@Au/Ni-Co) were used as ECL donors and exhibited excellent luminous efficiency. On the other hand, Pt nanoparticles-grown on copper sulphide (Pt@CuS) were used as energy acceptors to quench the initial signal based on RET between luminol and CuS. Moreover, the autonomous locomotion of I27L assisted by Exo III is the key in this DNA walker biosensor, as it continually induces new digestion processes on the electrode surface and quenches signals caused by the introduction of numerous acceptors. The efficient donor/acceptor pairs and DNA walker amplification system of the ECL-RET allowed the proposed biosensor to effectively detect I27L with a wide linear range of 0.0001 to 100 nM and a limit of detection as low as 23 fM. Thus, the ECL-RET biosensor provides a promising sensing platform for the diagnosis and typing of diabetes.

1. Introduction

Maturity-onset diabetes of the young (MODY) is a clinically heterogeneous group of monogenic and autosomal dominant disorders characterized by gene mutations that result in dysfunctional pancreatic islet β cells and subsequent insulin dysregulation [1,2]. According to the 2020 statistics by *Diabetes Gene* in the UK and *Standards of Medical Care in Diabetes of American Diabetes Association*, mutations in the hepatocyte nuclear factor-1α (HNF1A) genes are the most common causes of MODY. As a result, the detection of HNF1A mutant genes is the top priority in the diagnosis and etiological prediction of HNF1A-MODY [3,4]. Among the HNF1A mutant genes, common variants of I27L (rs1169288) are closely associated with monogenic susceptibility to diabetes [5]. Furthermore, I27L gene has the ability to reflect the function status of pancreatic islet β cell [6], has been identified as a marker for insulin resistance associated with increased risk of HNF1A-MODY mutations with an odds ratio of 1.5 [7,8]. Hence, developing new strategies with high sensitivity and specificity in the detection of I27L should be a priority for early monitoring and diagnosis of HNF1A-MODY.

Electrochemiluminescence resonance energy transfer (ECL-RET) is an important signal-off strategy that has been used in the analysis of trace amounts of different targets due to resonance energy transfer between efficient ECL emitters [9,10] and spectrally matched energy acceptors [11,12]. However, some typically ECL emitters (e.g. luminol, carbon dots, etc.) [13] are associated with drawbacks such as reagent waste, poor stability and the need for additional peroxidase [14]. These drawbacks can be overcome through efficient immobilization and effective catalysis of luminol, which would greatly improve the

* Corresponding authors.
E-mail addresses: yang623621810@163.com (W. Yang), luorongy@163.com (R. Luo).
[1] Wei Gong and Jia Shu contributed equally to this manuscript.

https://doi.org/10.1016/j.cej.2022.134681
Received 20 November 2021; Received in revised form 4 January 2022; Accepted 10 January 2022
Available online 13 January 2022

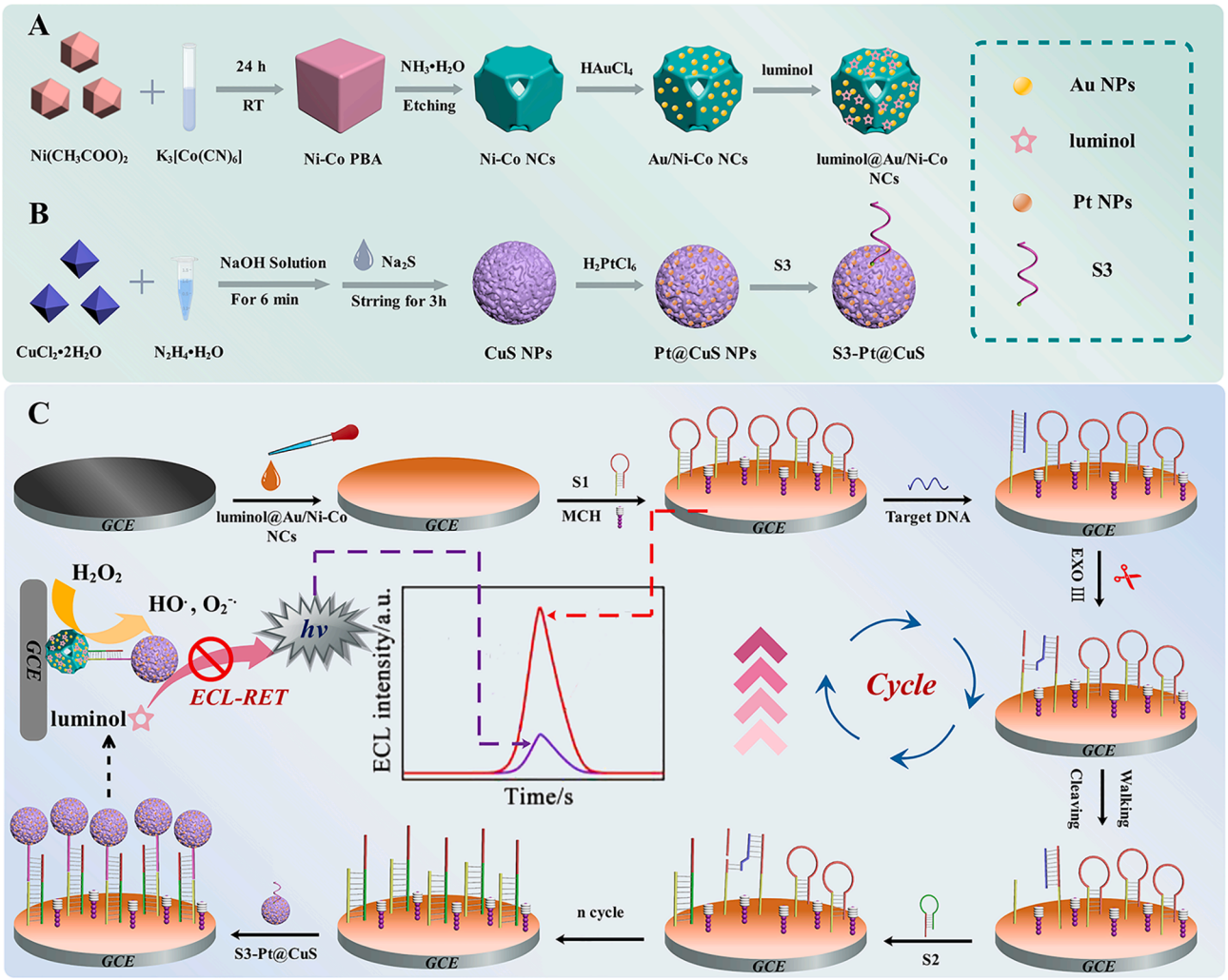

Scheme 1. Schematic illustration of ultrasensitive signal-off ECL biosensing using luminol@Au/Ni-Co NCs, Pt@CuS and stochastic DNA walkers for target DNA determination. (A) The synthesis protocol for luminol@Au/Ni-Co NCs. (B) The synthesis protocol for S3-Pt@CuS. (C) The process of movement and the mechanism of action of the DNA walking biosensor.

analytical performance of the ECL-RET strategy. Prussian blue analogues (PBAs) are a class of metal–organic frameworks (MOFs) characterized by open three-dimensional frameworks [15]. PBAs can be represented by the general formula $A^{II}_3[B^{III}(CN)_6]_2{\cdot}nH_2O$, where A and B refer to transition metals, such as Fe, Ni, Co, and Mn, linked by cyano ligands [16,17]. Additionally, the unique hollow and porous structures of PBAs enable the metal cations to be embedded at interstitial sites of the frameworks, resulting in excellent biocompatibility, selective adsorption properties and electrocatalytic activities. These properties indicate that PBAs have great potential as preeminent support matrixes and efficient catalysts [18,19]. Since PBAs have poor conductivity and rates of electron transport during the electrochemical process [20], they are usually combined with noble metallic nanoparticles (NPs), particularly Au NPs [21,22]. Based on these information, we synthesized luminol@Au/Ni-Co nanocages (NCs) (Scheme 1A), which could be used directly as ECL emitters and signal amplifiers for signal readout. More importantly, the addition of Ni-Co bimetallic nanozymes to luminol@Au/Ni-Co NCs greatly improves the luminescence efficiency of luminol, and ensures uniform dispersion of Au NPs that link to DNA strands via Au-S bonds.

The analytical performance of the ECL-RET strategy also depends on the degree of overlap between the energy donor emission spectrum and the acceptor excitation spectrum as well as the relative orientation of the electric dipoles for energy transfer between the donor and acceptor [23,24]. However, the small molecule dyes and plasmon nanoparticles currently used in ECL-RET strategies as energy acceptors are characterized by low electrochemical stability and energy transfer efficiency [25]. Therefore, the exploration of efficient energy acceptors is crucial to broaden the application of ECL-RET in biosensing analysis. Copper sulphide (CuS) is an excellent semiconductor that is regarded as one of the most promising high-performance ECL energy acceptors [26,27]. This is because it has unique absorption spectra in the visible light region, as well as superior electronic, physical and chemical properties [28]. For instance, Li et al generated CuS-reduced graphene oxide (CuS-rGO) on rGO in situ to detect N-terminal pro-brain natriuretic peptide (NT-proBNP). In this strategy, CuS was used as the energy acceptor to quench luminescence from luminol [29]. The ability of CuS to absorb light emitted by the luminol/H_2O_2 system at a wavelength of 425 nm, makes it a good quencher. We therefore synthesized CuS nanosphere-supported Pt NPs and single-stranded DNA bioconjugates (S3-Pt@CuS probes) (Scheme 1B) and used them as quenching probes to construct a signal-off ECL biosensing strategy.

To detect targets of low concentration with high sensitivity, we employed a target cycle amplification strategy by incorporating a novel stochastic DNA walker on the surface of electrode. DNA walkers are protein mimicking motors [30,31] that move automatically and continuously along the predesigned DNA tracks and are propelled by adding fuel strands or cleaving DNA or RNA strands with an enzyme

[32]. Currently, there are several studies on the use of hybridization chain reactions (HCR) [33], catalytic hairpin assembly (CHA) reaction [34], nicking endonuclease [35] and exonuclease III (Exo III) to fabricate DNA walking machines on the surface of 3D nanoparticles [36]. The toehold-exchange reaction has facilitated the development of hyper-specific conditional walking probes, making the amplification and detection of nucleic-acid or non-nucleic-acid targets in homogeneous solutions possible [37,38]. However, reagent waste, complex operation procedures and long response times still restrict their applications in ECL-RET immunoassays. Therefore, constructing a simple and efficient DNA walker that automatically moves DNA directly on the electrode surface is necessary. Based on the above analysis, we generated a free-walking single-stranded DNA target to act as a stochastic DNA walker. The walker was able to achieve target cycle amplification through repeated mechanical cycle movement along the DNA tracks composed of part or all of nucleic acids on the surface of electrode. Thus, the combination of DNA walker technology with ECL sensing can develop highly-efficient new biosensors.

Herein, we combined the advantages of luminol@Au/Ni-Co NCs, Pt@CuS and the stochastic DNA walking strategy to develop an innovative signal-off DNA walker biosensor for ultrasensitive detection of I27L. As shown in Scheme 1C, luminol@Au/Ni-Co NCs were applied onto the surface of glassy carbon electrode (GCE) to act as ECL donors. Thereafter, a stem-loop structural hairpin DNA (S1) was linked to luminol@Au/Ni-Co NCs through Au-S bonds, which was later opened in the presence of target DNA (I27L, H) to form S1: target DNA duplex. Subsequently, the S1: target DNA duplex formed was cleaved using Exo III, resulting in the stochastic movement of target DNA. Noteworthy, Exo III selectively cleaved the double-stranded DNA from the 3'-OH blunt or concave end with little effect on the single stranded DNA [39], thus acting as a promoter in this DNA walker system. The target DNA opened the hairpin structure of S1 as it moved, allowing the capture probe (S2) to hybridize with S1. The detection of I27L with high sensitivity and specificity was achieved by capturing numerous S3-Pt@CuS probes as ECL acceptor quenchers.

2. Experimental section

2.1. Synthesis of luminol@Au/Ni-Co NCs

Ni-Co PBAs was synthesized according to a previous report with slight modifications [40]. $Ni(CH_3COO)_2$ (0.0745 g) and 0.132 g of sodium citrate were dissolved in 10 mL of deionized (DI) water to form a light green clear solution. The solution was then added dropwise to 10 mL of 19.98 mM $K_3[Co(CN)_6]$ solution, stirred vigorously for 5 min and left for 24 h at room temperature. Subsequently, the mixture was centrifuged at 9000 rpm for 5 min to collect Ni-Co PBAs, which were then washed three times using ultrapure water and dried in a vacuum at 80 °C overnight. Afterwards, 10 mL of H_2O containing 2.5 mL of $NH_3{\cdot}H_2O$ was added into 5 mL of ethanol containing 10 mg of Ni-Co PBAs and stirred for 5 min at room temperature to obtain the Ni-Co NCs. The precipitate was collected by centrifugation, washed with DI water and ethanol, and then dried at 75 °C overnight.

The synthesized Ni-Co NCs were completely dissolved in 20 mL

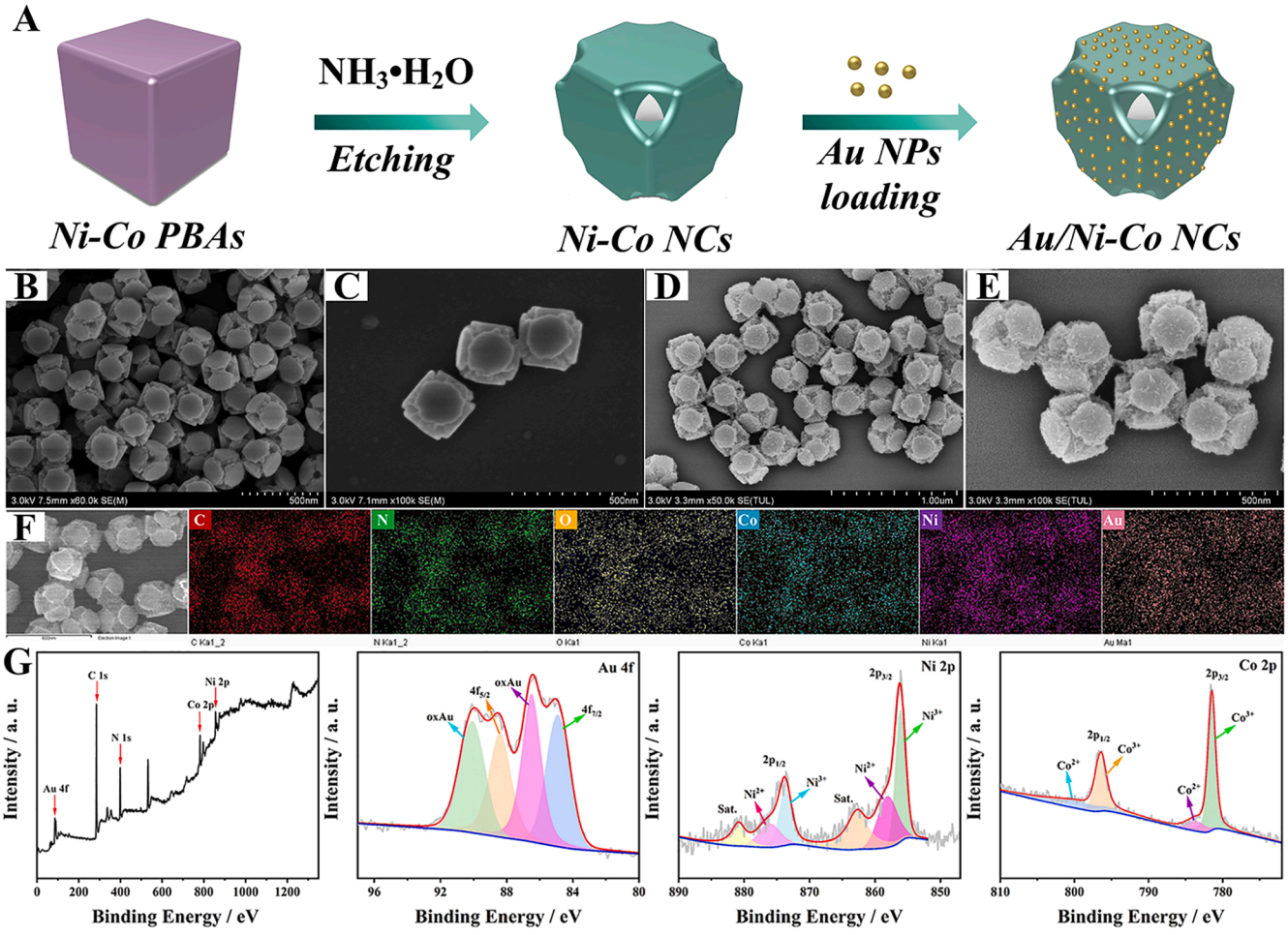

Fig. 1. Schematic diagram for the fabrication of Au/Ni-Co NCs (A), SEM imagines of Ni-Co NCs (B and C), Au/Ni-Co NCs (D and E), SEM-EDS mappings of Au/Ni-Co NCs (F), XPS high resolution spectra of Au/Ni-Co NCs (G).

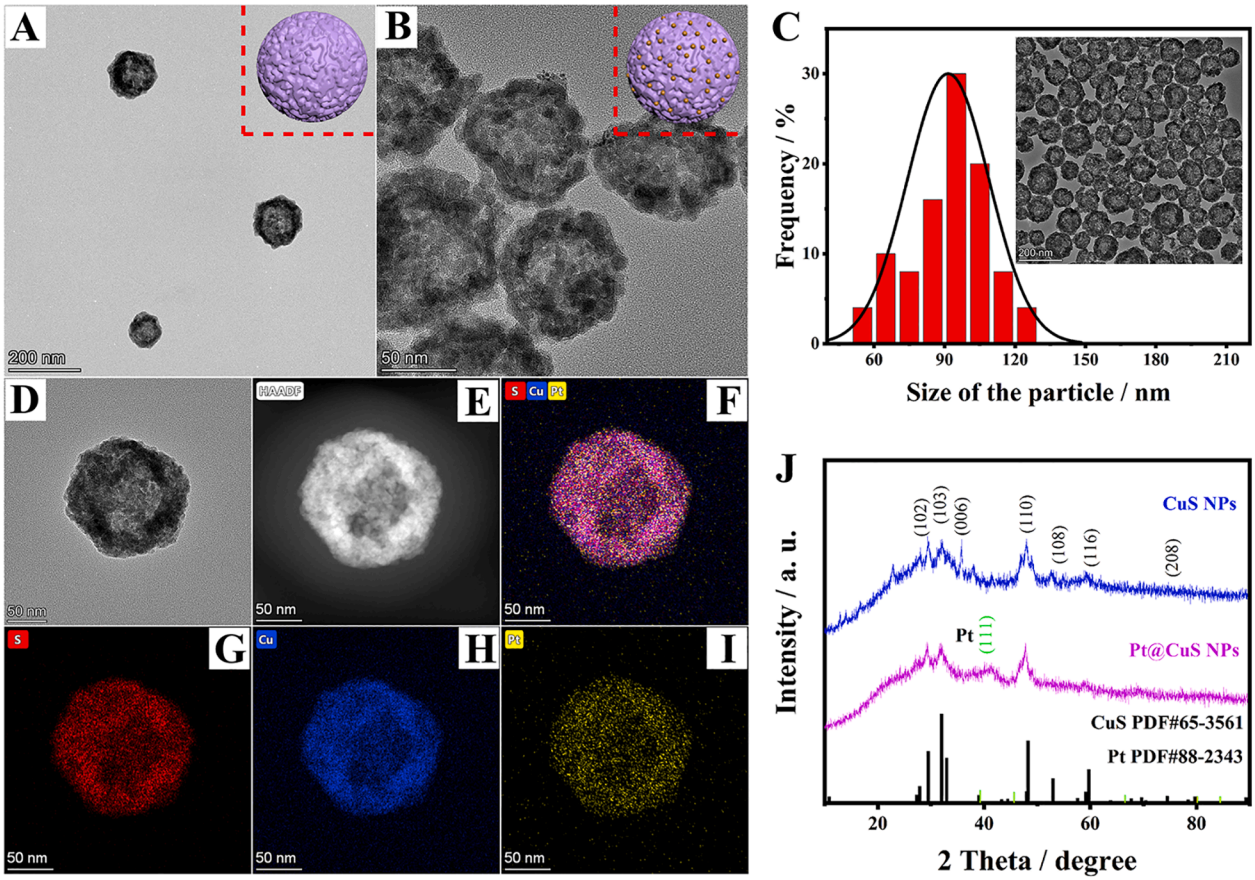

Fig. 2. TEM imagines of CuS NPs (A), Pt@CuS (B and D); Size distribution of the Pt@CuS nanospheres (C); High-angle annular dark-field (HAADF)-TEM-EDS mappings of Pt@CuS (E-I); XRD pattern of CuS NPs and Pt@CuS (J).

absolute ethanol by stirring for 10 min. Thereafter, 250 uL of $HAuCl_4{\cdot}6H_2O$ (1.0 wt%) was added to the Ni-Co NCs suspension and stirred continuously for 30 min. After that, 10 uL of fresh 1.9 M $NaBH_4$ was quickly added to the mixture while stirring vigorously. The appearance of a purplish red color in the solution was an indication that Au NPs had been formed. After 30 min, the resultant Au/Ni-Co NCs were harvested, repeatedly washed with deionized water and re-suspended in 20 mL DI water. Luminol@Au/Ni-Co was generated by adding 1 mL of 10 mM luminol to the Au/Ni-Co NCs solution and stirring for 6 h. Finally, the resultant mixture was centrifuged and washed to remove uncombined luminol molecules. The luminol@Au/Ni-Co NCs were re-suspended in 0.2 % chitosan solution and stored at 4 °C for later use.

2.2. Preparation of S3-Pt@CuS bioconjugates

CuS NPs were synthesized according to a previously published protocol but with slight modifications [41]. 100 uL of 0.5 M $CuCl_2{\cdot}2H_2O$ was added to 25 mL DI water containing 0.24 g PVP-K30 under magnetic stirring at 30 °C. Thereafter, 25 mL NaOH solution (pH = 9.0) and 6.4 μL $N_2H_4{\cdot}H_2O$ was added sequentially to form a bright-yellow suspension of Cu_2O spheres, which was added with 200 μL of 1.3 M $Na_2S{\cdot}9H_2O$ aqueous solution after stirring for 6 min. The solution was then heated for 2 h at 60 °C. Lastly, CuS NPs were centrifuged at 12000 rpm for 10 min, washed three times with DI water and ethanol, and resuspended in 2 mL ethanol.

Afterwards, 1 mL of the CuS NPs solution prepared was mixed with 8 mL ethanol and 0.01 g PVP-K30 under magnetic stirring for 30 min. Then, 9.6 mL of 0.3 mM $H_2PtCl_6{\cdot}6H_2O$ aqueous solution was added to the mixture and stirred for an additional 10 min. Subsequently, the mixture was mixed with 0.5 mL of 3 mM $NaBH_4$ aqueous solution, stirred for 30 min, and centrifuged at 12000 rpm for 10 min to obtain Pt@CuS. Next, the Pt@CuS obtained was washed three times with ethanol and DI water. The S3-Pt@CuS bioconjugates rely mainly on the platinum-ammonia bonds formed between the amino group at the 3′ end of S3 sequence and Pt NPs. First, 200 μL of 10 μM S3 solution and an equal volume of Pt@CuS were mixed together and oscillated overnight at 4 °C, to allow the effective binding of S3 to Pt@CuS. The mixture was then incubated at 37 °C for 4 h. Finally, the solution was centrifuged several times in a buffer to acquire S3-Pt@CuS bioconjugates, which were stored at −20 °C until further use.

2.3. Electrode modification and pretreatment

Prior to modification, the bare GCE was polished sequentially with 0.3 μm and 0.05 μm alumina power, and then rinsed ultrasonically with ethanol and DI water. Subsequently, 10 μL of luminol@Au/Ni-Co was applied to the surface of bare GCE and dried at 37 °C. Then, 10 μL of S1 (1 μM) was applied on the luminol@Au/Ni-Co NCs/GCE and incubated at 4 °C overnight. Thereafter, the luminol@Au/Ni-Co decorated electrode was rinsed and any remaining non-specific sites blocked by incubating with 4 μL of 1 mM MCH at 4 °C for 40 min. Before incubation, the S1 sequence was activated using TCEP to break the S-S bond. Lastly, the MCH/S1/luminol@Au/Ni-Co/GCE was thoroughly flushed with a buffer solution for subsequent use.

2.4. Walking process of DNA walker and ECL detection of I27L

The walking process of the DNA walker is shown in Scheme 1C. First, 10 μL target DNA (H) at different concentrations were dropped into the luminol@Au/Ni-Co modified electrode surface and incubated for 1 h at

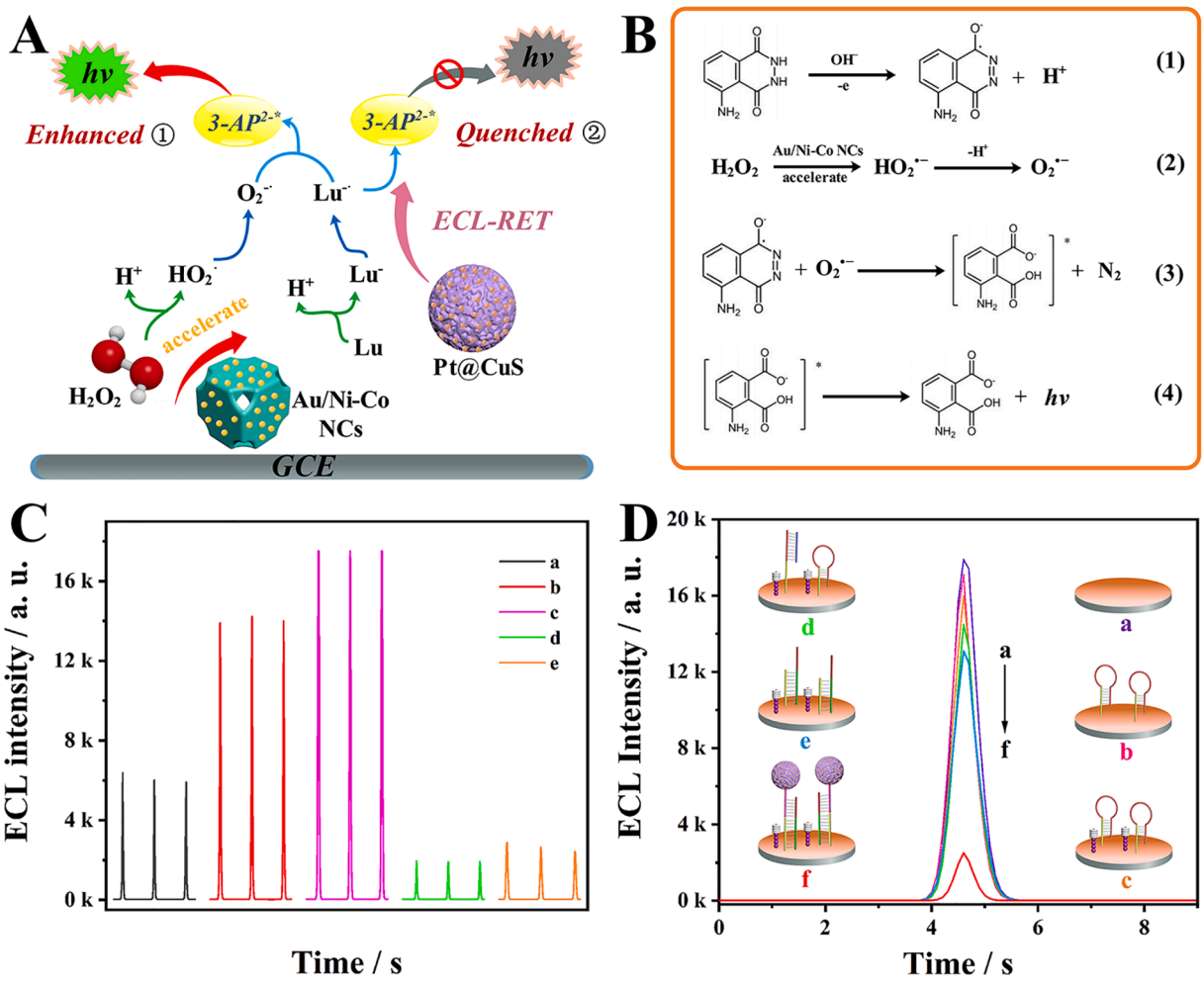

Fig. 3. (A) Schematic illustration for the possible mechanisms of ECL sensing strategy; (B) Possible ECL reaction equation of luminol@Au/Ni-Co NCs system; (C) ECL signals emitted by luminol (a), Ni-Co NCs@luminol (b), luminol@Au/Ni-Co NCs (c), CuS NPs/luminol@Au/Ni-Co NCs (d), and Pt@CuS/luminol@Au/Ni-Co NCs (e); (D) ECL signals emitted by (a) luminol@Au/Ni-Co NCs/GCE, (b) luminol@Au/Ni-Co NCs/GCE incubated with strands S1, (c) MCH/S1/luminol@Au/Ni-Co NCs/GCE, (d) MCH/S1/luminol@Au/Ni-Co NCs/GCE incubated with 10 nM target DNA: H, (e) S2/H/MCH/S1/luminol@Au/Ni-Co NCs/GCE, (f) e incubated with S3-Pt@CuS.

37 °C. Thereafter, 10 μL of 0.8 U μL^{-1} Exo III solution was dropped onto the H/MCH/S1/luminol@Au/Ni-Co/GCE surface and the walking process of the DNA walker allowed to take place for 50 min. After cleaning thoroughly, 10 μL of 1 μM S2 was placed onto the electrode surface and incubated for 1 h at 37 °C. Finally, 10 μL S3-Pt@CuS bioconjugates were incubated with the modified electrode for 2 h to load the Pt@CuS quencher on the luminol@Au/Ni-Co/GCE surface. The quenching of the ECL signal allowed the detection of I27L.

3. Results and discussion

3.1. Characterization of Ni-Co NCs and Au/Ni-Co nanocomposites

The morphology and elemental composition of the synthesized nanoparticles were characterized using SEM technology and SEM-EDS elemental mapping. As depicted in Fig. 1B and Fig. 1C, the SEM image showed a hollow nanocube structure with obvious openings of about 250 nm at each corner of Ni Co NCs. Analysis of the Au NPs-modified Ni-Co NCs showed that the hollow open structure allowed the homogeneous dispersion of Au NPs on the surface of Ni-Co NCs (Fig. 1D and Fig. 1E). Meanwhile, SEM-EDS mapping was used to identify the corresponding distribution of C, N, O, Ni, Co and Au elements (Fig. 1F). The results of the mapping revealed that Au nanoparticles were uniformly dispersed on the surface of the Ni-Co NCs.

XPS was used to analyze the chemical bonding, electronic state and elementary composition of the Au/Ni-Co NCs surface. The XPS survey spectrum of Au/Ni-Co NCs shown in Fig. 1G indicates that the surface of the nanocages mainly contained Au, Ni, and Co. The Au 4f spectrum could be best fitted by Au $4f_{7/2}$ and Au $4f_{5/2}$ located at 84.2 eV and 87.9 eV accompanied by two satellite peaks, indicating formation of Au nanoparticles on the surface of Ni-Co NCs [42]. The binding energies at 854.7 and 872.2 eV corresponded to Ni^{3+}, while the energies at 856.1 and 873.4 eV were attributed to Ni^{2+}. This confirmed the existence of Ni^{2+} and Ni^{3+} [43]. As demonstrated in the high-resolution spectra of Co 2p, the two major peaks located at 781.3 eV and 796.6 eV corresponded to Co $2p_{3/2}$ and Co $2p_{1/2}$, together with two shake-up satellite peaks [44].

XRD was also used to investigate the crystal structures of Ni-Co NCs and Au/Ni-Co NCs. As illustrated in Fig. S1, the diffraction peaks of Au/Ni-Co NCs coincided exactly with Ni-Co NCs, and all the diffraction peaks can be indexed to the $Ni_3[Co(CN)_6]_2{\cdot}12H_2O$ (PDF card: JCPDS 89–3738) [45]. This result suggested that the nanocage still maintained a stable Prussian-blue-like crystal structure during the synthesis of Au/Ni-Co NCs. The absence of XRD peaks from Au NPs was probably due to the low concentration as well as the small size of the Au NPs applied on the Ni-Co nanocages.

3.2. Characterization of CuS NPs and Pt@CuS

TEM scanning electron microscopy was used to characterize the

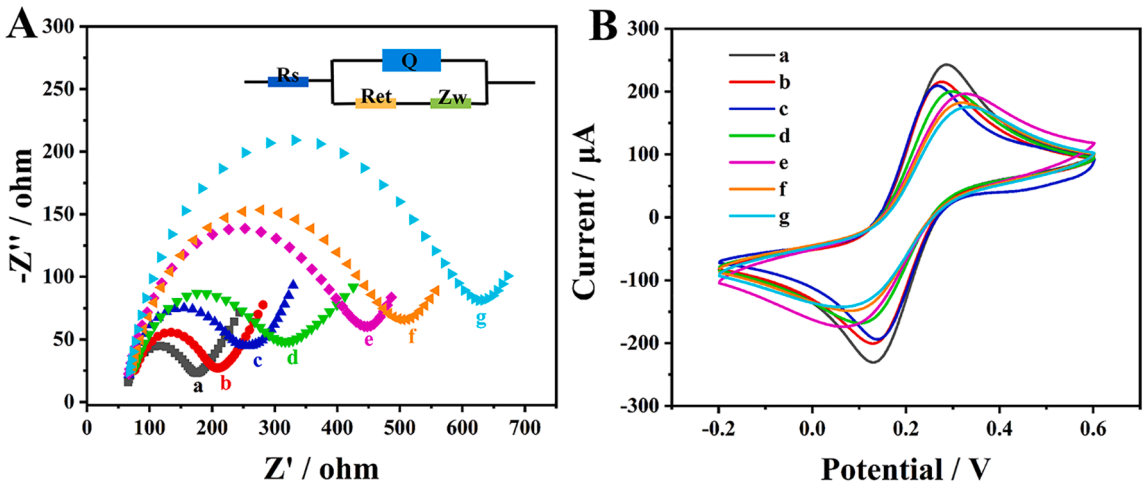

Fig. 4. (A) EIS and (B) CV curves during the stepwise modification process measured in 5.0 mM $[Fe(CN)_6]^{3-/4-}$ solution containing 0.1 M KCl.

morphology of CuS NPs and Pt@CuS. As shown in Fig. 2A, CuS NPs consisted of highly dispersed and uniform nanospheres with an average diameter of 90 nm (Fig. 2C). Analysis of the Pt-modified CuS NPs showed that the spherical Pt nanoparticles were uniformly deposited on the surface of CuS NPs to form a nanoshell morphology (Fig. 2B). The Pt@CuS components were further confirmed through high-angle annular dark-field transmission electron microscopy (HAADF-TEM) and EDS mapping analysis (Fig. 2E-I). From the results, there was evidence of the existence of Pt, Cu and S elements in Pt@CuS. This suggested that the Pt nanoparticles with spherical configuration were uniformly distributed on the surface of CuS NPs.

XRD analysis revealed that CuS and Pt@CuS consisted of crystalline structures. Characterization of the XRD patterns of CuS NPs and Pt@CuS showed that the two nanomaterials produced a series of diffraction peaks located at 29.48°, 31.99°, 32.96°, 48.31°, 52.97°, 59.72° and 74.49° (Fig. 2J). These seven peaks corresponded to the (102), (103), (006), (110), (108), (116) and (208) crystalline planes of CuS (PDF card: JCPDS 65–3561) [46]. In addition, there was a broad peak at around 39.27° (marked with green labels) in the XRD pattern of Pt@CuS, which could be obviously indexed to the (111) crystal plane of Pt (PDF card: JCPDS 88–2343), suggesting successful assembly of Pt NPs on CuS nanospheres. These findings strongly demonstrated the successful synthesis of Pt@CuS composites.

3.3. Possible mechanisms underlying the ECL sensing strategy

In Fig. 3A, we illustrate our proposed strategy for signal enhancement and quenching mechanism of the fabricated ECL biosensor. First, luminol was oxidized to luminol anion (eq (1) in Fig. 3B) under the scan of a positive potential on the surface of electrode. Thereafter, Au/Ni-Co NCs catalyzed the reduction of H_2O_2 to $O_2^{\bullet-}$ on the surface of the electrode (eq (2) in Fig. 3B). Further on, the luminol anion reacted with $O_2^{\bullet-}$ to produce a luminol anion in the excited state (eq (3) in Fig. 3B), which returned to the ground-state luminol anion after emitting light (eq (4) in Fig. 3B). Additionally, ECL curves of various materials were recorded in PBS (0.1 M, pH 8.0) containing 10 mM H_2O_2 to make our report explicit. As exhibited in Fig. 3C, the presence of luminol/GCE in H_2O_2 generated a distinct ECL signal with an intensity of about 6000 a.u. (Fig. 3C, curve a). This was indication that H_2O_2 could react with luminol to amplify the ECL signal. The application of Ni-Co NCs to GCE surface increased the ECL intensity when compared with luminol/GCE (6000 to 14,000 a.u.) (Fig. 3C, curve b). The addition of Au NPs to Ni-Co NCs@luminol to form luminol@Au/Ni-Co NCs/GCE, further increased the signal from 14,000 to 17,000 a.u. (Fig. 3C, curve c). This suggested that the synthesized luminol@Au/Ni-Co NCs had superior catalytic activity. Importantly, the addition of CuS NPs to luminol@Au/Ni-Co NCs/GCE system caused a significant decrease in the ECL signal (from 17,000 to 2000 a.u.) (Fig. 3C, curve d). This demonstrated that CuS NPs can act as energy acceptors to quench the excited states of ECL emitters. Additionally, there was no significant difference in ECL intensities between Pt@CuS/luminol@Au/Ni-Co NCs/GCE (Fig. 3C, curve e) and CuS/luminol@Au/Ni-Co NCs/GCE, suggesting that Pt NPs had little effect on the quenching activity of CuS NPs.

The UV–Vis absorbance spectra of S3 sequence, CuS NPs, Pt@CuS and S3-Pt@CuS were monitored to determine if the S3 sequence had been successfully assembled on the Pt@CuS composite surface (Fig. S2). An absorption peak at 260 nm, characteristic of nucleotides (S3 strands), was observed in the UV–Vis absorption spectra of S3-Pt@CuS bioconjugates, indicating successful preparation of S3-Pt@CuS bioconjugates. Meanwhile, we also analyzed the ECL signals during the stepwise electrode modification process Fig. 3D. The application of luminol@Au/Ni-Co NCs on the surface of GCE generated a significant signal at the beginning of the process (Fig. 3D, curve a), suggesting that Au/Ni-Co NCs accelerated H_2O_2 decomposition to enhance ECL intensity. Subsequent immobilization of S1 (Fig. 3D, curve b), MCH (Fig. 3D, curve c), target DNA (Fig. 3D, curve d), and S2 (Fig. 3D, curve e) on the surface of luminol@Au/Ni-Co NCs modified electrode slightly decreased the ECL signal. This was because the insulating nucleotide impeded electron transfer between luminophore and H_2O_2. Moreover, it is worth mentioning that ECL intensity decreased remarkably from 12,000 to 2000 a.u. (Fig. 3D, curve f) when S3-Pt@CuS bioconjugates were applied on GCE. Based on the mechanism we had proposed earlier, we speculated that the amplified ECL signal was effectively quenched through RET between an efficient ECL emitter and a spectrally matched energy acceptor (Pt@CuS). These results demonstrated that the assembled DNA walker moved successfully on the electrode surface.

3.4. Characterization of the prepared DNA walking biosensor

Electrochemical impedance spectroscopy (EIS) and cyclic voltammetry (CV) experiment are extensive and powerful tools for characterizing the changes in the sensor interface during the modification and assembly of the electrodes. As displayed in Fig. 4A, the bare GCE exhibited a relatively minor semicircle diameter of EIS Nyquist plot (curve a), demonstrating faster electron transfer on the electrode surface. The application of luminol@Au/Ni-Co NCs on the surface of the electrodes caused a slight increase in the diameter of the semicircle (curve b) due to low conductivity of chitosan and Ni-Co NCs. Further, immobilization of S1 strands caused significant increase in the diameter of the semicircle due to the increased distance for electron transfer

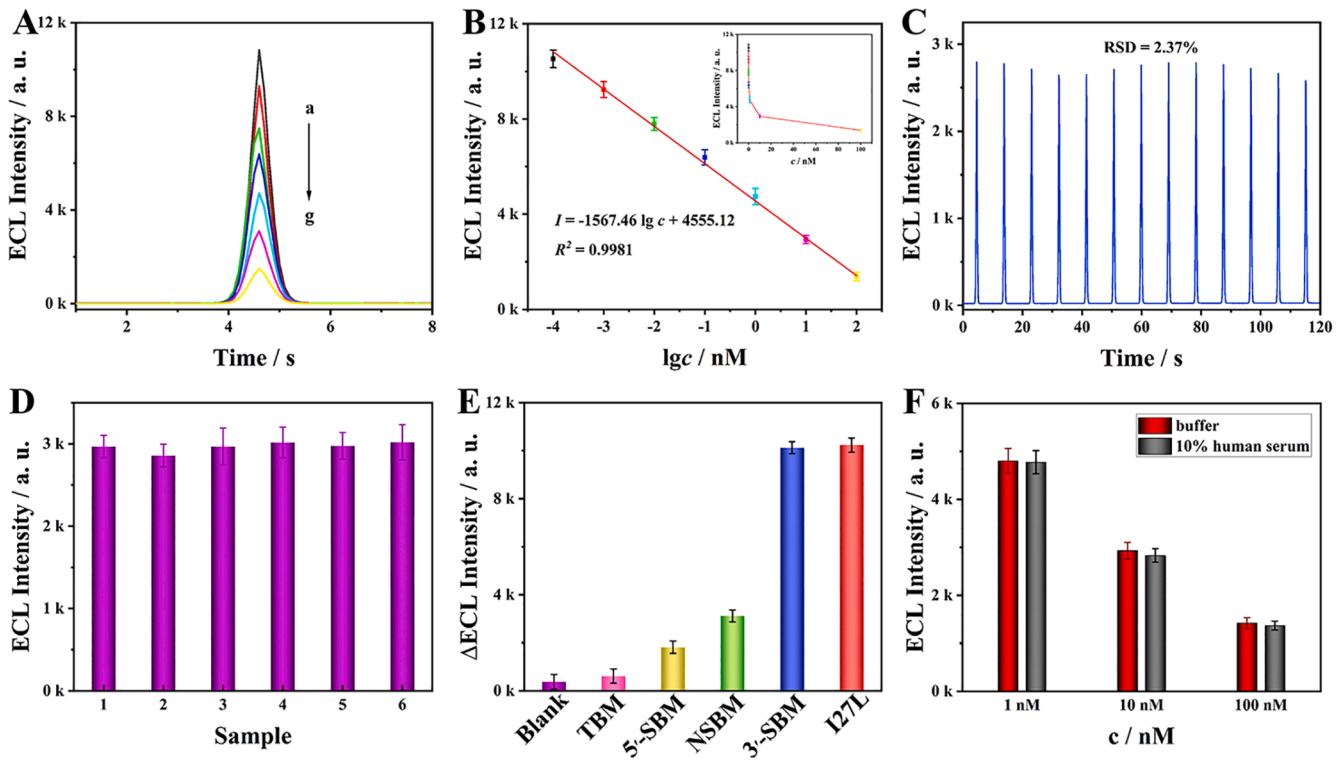

Fig. 5. (A) ECL intensity-time curves of the fabricated ECL biosensor with different concentrations of target DNA (from a to g: 0.0001, 0.001, 0.01, 0.1, 1, 10, 100 nM); (B) The linear relationship between ECL intensities and the logarithms of target DNA concentrations; (C) Stability of the biosensor in detecting 10 nM target DNA; (D) Reproducibility of the biosensor in detecting 10 nM target DNA in six individual tests; (E) Selectivity of the biosensor against oligonucleotides of different sequences. The concentrations of TBM, 5'-SBM, NSBM, 3'-SBM, and I27L are 10 nM. (F) Comparison of target DNA detection in buffer and 10% serum samples by the proposed DNA walking biosensor (Error bars, SD, n = 3).

Table 1
Comparison of linear ranges and detection limits of the different electrochemical DNA sensors.

Modified electrodes	Detection technique	Linear range (nM)	Detection limit (fM)	References
ZrO_2/Au/GCE	DPV	0.225–22.5	1×10^5	[47]
Au–MPA–Zr (IV)	EIS	0.1–1000	8.5×10^4	[48]
CeO_2/CHIT/GC	DPV	0.0159–116	1×10^4	[49]
acpcPNA/PAD	EIS	2–200	1.24×10^6	[50]
4-ATP/NG/Au	DPV	0.014–2	9.5×10^3	[51]
Au/Ni-Co NCs/GCE	ECL	0.0001–100	23	This work

caused by negatively charged phosphate groups in the oligonucleotides (curve c). The successive introduction of MCH (curve d), target DNA: H (curve e), and S2 (curve f) resulted in further increase in resistance, which was attributed to the electrostatic repulsion between abundant negative charges of DNA sequence and electroactive $[Fe(CN)_6]^{3-/4-}$. Furthermore, when S3-Pt@CuS bioconjugates were attached to the modified electrode, the resistance value greatly increased (curve g) because the deposited insulator hindered electron transfer. These results were validated using a CV experiment (Fig. 4B), suggesting the successful fabrication of a DNA walking biosensor.

3.5. Analytical performance of ECL biosensor towards I27L

The DNA walking biosensor generated was used to detect different concentrations of I27L ranging from 0.0001 nM to 100 nM (curve a-g in Fig. 5A) under optimal conditions (*Supporting Information*). As shown in the calibration plots of Fig. 5B, the ECL intensity was logarithmically related to the concentrations of I27L ranging from 0.0001 nM to 100 nM. The linear regression equation was expressed as I = -1567.46 lg c + 4555.12 with a correlation coefficient of R^2 = 0.9981. The limit of detection (LOD) was calculated to be 23 fM according to the international union of pure and applied chemistry (IUPAC). Our stochastic DNA walker ECL biosensor exhibited a wider dynamic detection range and lower detection limit for the target DNA assay compared to other DNA sensors that have been reported (Table 1), which ascribed the efficient quenching advantages of abundant S3-Pt@CuS probes driven by stochastic DNA walker recycling. The excellent electrocatalytic performance of Au/Ni-Co NCs combined with the high signal quenching ability of Pt@CuS probes, generated a biosensor able to effectively detect target DNA and with promising application in clinical settings.

3.6. Stability, reproducibility and specificity of the biosensor

The stability of the biosensor and the synthesized luminophore nanomaterials was one of the major concerns in evaluating whether the biosensor can be applied in practice. As shown in Fig. 5C, 10 nM target DNA was able to generate a steady ECL signal under 13 cycles of continuous scans with an average relative standard deviation (RSD) of 2.37%. Meanwhile, luminol@Au/Ni-Co NCs composites also generated stable ECL signals with a RSD of 1.41% in Fig. S4. Additionally, the DNA walking biosensor was monitored by recording ECL response during storing at 4 °C. The initial signal response remained 92.46% after 12 days (Fig.S5), indicating acceptable stability of the biosensor.

We also assessed the reproducibility of the biosensor by analyzing six identical electrodes under the same reaction condition. In this assay, 10 nM target DNA was used as the model target and the average coefficient of variation (CV) among the six electrodes was 1.81 (Fig. 5D). These results indicated that the ECL strategy for target DNA detection exhibited acceptable reproducibility.

Table 2
Analytical application of the biosensor in diluted human serum samples.

Sample	Addition (nM)	ECL intensity (a. u.)	Found (nM)	RSD (%, n = 3)	Recovery (%, n = 3)
1	100.00	1427.66	98.91	6.77	98.91
2	10.00	2975.92	10.174	4.98	101.74
3	1.00	4556.34	0.9982	5.04	99.82

To investigate the specificity of the proposed ECL biosensor, we analyzed the ECL signals generated by high concentrations (10 nM) of five oligonucleotides with different sequences. The oligonucleotides included target DNA (I27L), non-terminal single-base mismatch (NSBM), 5' end single-base mismatch (5'-SBM), 3' end single-base mismatch (3'-SBM) and three-bases mismatch (TBM) (Fig. 5E). There were very few changes in signal observed in the blank solution and TBM sequences, while a relatively small change in ΔECL intensity was observed in NSBM sequences. Additionally, we observed the effect of a single-base mismatch at the 5' and 3' ends of the DNA. The single-base mismatch at the 5' end slowed the DNA walking process due to the difficulty in opening hairpin chain S1, resulting in a weak ΔECL signal change. However, the effect of single-base mismatch at 3' end on ECL signal was insignificant as the supernumerary bases at the 3' end of target DNA were not involved in the hybridization reaction with S1. These findings were a reflection of the excellent selectivity of our ECL biosensor.

3.7. Detection of I27L in human serum samples

In order to assess the applicability and reliability of the DNA walking biosensor, we used the standard spike-and-recovery method to detect I27L in diluted human serum samples. Human serum was first diluted 10 times with PBS (0.01 M, pH 7.4) buffer to obtain a 10% serum solution, which was then used as a buffer to detect target DNA. As illustrated in Fig. 5F, the ECL signal measured in the 10% serum samples was nearly the same as that in the buffer. The recoveries were between 98.91% and 101.74% with RSD ranging from 4.98% to 6.77% (Table 2). This demonstrated the potential of the DNA walking biosensor in the analysis of DNA in complex clinical samples.

4. Conclusion

In this research, a signal-off ECL biosensing strategy was fabricated using luminol@Au/Ni-Co NCs as the ECL donors and Pt@CuS as the synergistic energy acceptor. Target DNA-induced stochastic DNA walker recycling was used for signal amplification for ultrasensitive detection of I27L gene. The fabricated luminol@Au/Ni-Co NCs had multiple functions such as mimicking peroxidase, and acting as nanocarriers as well as ECL donors. This greatly boosted the luminous performance and provided more active sites for binding DNA strands. Meanwhile, signal amplification was achieved by using target DNA as stochastic walkers to develop Exo III-assisted DNA walking system. This enabled effective quenching of the initial amplified signal by Pt@CuS acceptor through the ECL-RET strategy. The ECL biosensor was not only precise in quantitative analysis of the I27L gene, but it also provided a general platform for the detection of other DNA or RNA molecules. In our future work, we will focus on simplifying the procedures for synthetizing luminol@Au/Ni-Co NCs and exploring more ECL donors and acceptors. In conclusion, this signal-off ECL biosensing strategy offers a sensing interface to achieve efficient signal amplification and a platform for nucleic acid detection in clinical settings.

Declaration of Competing Interest

The authors declare that they have no known competing financial interests or personal relationships that could have appeared to influence the work reported in this paper.

Acknowledgements

This research was funded by the financial support from the National Science and Technology Major Project of the Ministry of Science and Technology of China (2018ZX10732202), and the National Natural Science Foundation of China (81873980).

Appendix A. Supplementary data

Supplementary data to this article can be found online at https://doi.org/10.1016/j.cej.2022.134681.

References

[1] H. Al-Kandari, D. Al-Abdulrazzaq, L. Davidsson, F. Al-Mulla, Maturity-onset diabetes of the young (MODY): a time to act, Lancet Diabetes Endocrinol. 8 (7) (2020) 565–566, https://doi.org/10.1016/s2213-8587(20)30150-9.
[2] S.R. Johnson, H.E. Carter, P. Leo, S.A. Hollingworth, E.A. Davis, T.W. Jones, L. S. Conwell, M. Harris, M.A. Brown, N. Graves, E.L. Duncan, Cost-effectiveness analysis of routine screening using massively parallel sequencing for maturity-onset diabetes of the young in a pediatric diabetes cohort: reduced health system costs and improved patient quality of life, Diabetes Care 42 (1) (2019) 69–76, https://doi.org/10.2337/dc18-0261.
[3] H. Zhang, K. Colclough, A.L. Gloyn, T.I. Pollin, Monogenic diabetes: a gateway to precision medicine in diabetes, J. Clin. Invest. 131 (3) (2021), https://doi.org/10.1172/JCI142244.
[4] G. Thanabalasingham, K.R. Owen, Diagnosis and management of maturity onset diabetes of the young (MODY), BMJ 343 (2011) d6044. https://doi.org/10.1136/bmj.d6044.
[5] J. Holmkvist, C. Cervin, V. Lyssenko, W. Winckler, D. Anevski, C. Cilio, P. Almgren, G. Berglund, P. Nilsson, T. Tuomi, C.M. Lindgren, D. Altshuler, L. Groop, Common variants in HNF-1 alpha and risk of type 2 diabetes, Diabetologia 49 (12) (2006) 2882–2891, https://doi.org/10.1007/s00125-006-0450-x.
[6] K.C. Chiu, L.-M. Chuang, J.M. Ryu, G.P. Tsai, M.F. Saad, The I27L Amino Acid Polymorphism of Hepatic Nuclear Factor-1α Is Associated with Insulin Resistance1, J. Clin. Endocrinol. Metab. 85 (6) (2000) 2178–2183, https://doi.org/10.1210/jcem.85.6.6618.
[7] K.C. Chiu, L.M. Chuang, A. Chu, C. Yoon, M. Wang, Comparison of the impact of the I27L polymorphism of the hepatocyte nuclear factor-1alpha on estimated and measured beta cell indices, Eur. J. Endocrinol. 148 (6) (2003) 641–647, https://doi.org/10.1530/eje.0.1480641.
[8] J. Holmkvist, P. Almgren, V. Lyssenko, C.M. Lindgren, K.F. Eriksson, B. Isomaa, T. Tuomi, P. Nilsson, L. Groop, Common variants in maturity-onset diabetes of the young genes and future risk of type 2 diabetes, Diabetes 57 (6) (2008) 1738–1744, https://doi.org/10.2337/db06-1464.
[9] B. Wang, H. Song, X. Qu, J. Chang, B. Yang, S. Lu, Carbon dots as a new class of nanomedicines: Opportunities and challenges, Coordin. Chem. Rev. 442 (2021) 214010, https://doi.org/10.1016/j.ccr.2021.214010.
[10] B. Wang, J. Yu, L. Sui, S. Zhu, Z. Tang, B. Yang, S. Lu, Rational Design of Multi-Color-Emissive Carbon Dots in a Single Reaction System by Hydrothermal, Adv. Sci. 8 (1) (2021) 2001453, https://doi.org/10.1002/advs.202001453.
[11] Z. Fan, B.o. Yao, Y. Ding, D. Xu, J. Zhao, K. Zhang, Rational engineering the DNA tetrahedrons of dual wavelength ratiometric electrochemiluminescence biosensor for high efficient detection of SARS-CoV-2 RdRp gene by using entropy-driven and bipedal DNA walker amplification strategy, Chem. Eng. J. 427 (2022) 131686, https://doi.org/10.1016/j.cej.2021.131686.
[12] B. Babamiri, D. Bahari, A. Salimi, Highly sensitive bioaffinity electrochemiluminescence sensors: Recent advances and future directions, Biosens. Bioelectron. 142 (2019) 111530, https://doi.org/10.1016/j.bios.2019.111530.
[13] B. Wang, J. Li, Z. Tang, B. Yang, S. Lu, Near-infrared emissive carbon dots with 33.96% emission in aqueous solution for cellular sensing and light-emitting diodes, Science Bulletin 64 (17) (2019) 1285–1292.
[14] W. Yang, Q. Peng, Z. Guo, H. Wu, S. Ding, Y. Chen, M. Zhao, PtCo nanocubes/reduced graphene oxide hybrids and hybridization chain reaction-based dual amplified electrochemiluminescence immunosensing of antimyeloperoxidase, Biosens. Bioelectron. 142 (2019) 111548, https://doi.org/10.1016/j.bios.2019.111548.
[15] C. Xu, Z. Yang, X. Zhang, M. Xia, H. Yan, J. Li, H. Yu, L. Zhang, J. Shu, Prussian Blue Analogues in Aqueous Batteries and Desalination Batteries, Nano-micro Lett. 13 (1) (2021) 166, https://doi.org/10.1007/s40820-021-00700-9.
[16] J. Nai, X.W.(. Lou, Hollow Structures Based on Prussian Blue and Its Analogs for Electrochemical Energy Storage and Conversion, Adv. Mater. 31 (38) (2019) 1706825, https://doi.org/10.1002/adma.201706825.
[17] L. Han, X.-Y. Yu, X.W.D. Lou, Formation of Prussian-Blue-Analog Nanocages via a Direct Etching Method and their Conversion into Ni-Co-Mixed Oxide for Enhanced Oxygen Evolution, Adv. Mater. 28 (23) (2016) 4601–4605, https://doi.org/10.1002/adma.201506315.
[18] M.A. Lumley, D.-H. Nam, K.-S. Choi, Elucidating Structure–Composition–Property Relationships of Ni-Based Prussian Blue Analogues for Electrochemical Seawater

Desalination, ACS Appl. Mater. Interfaces 12 (32) (2020) 36014–36025, https://doi.org/10.1021/acsami.0c0808410.1021/acsami.0c08084.s001.
[19] B. Singh, O. Prakash, P. Maiti, P.W. Menezes, A. Indra, Electrochemical transformation of Prussian blue analogues into ultrathin layered double hydroxide nanosheets for water splitting, Chem. Commun. 56 (95) (2020) 15036–15039, https://doi.org/10.1039/D0CC06362B.
[20] Q.i. Zhang, L. Li, Z. Qiao, C. Lei, Y. Fu, Q. Xie, S. Yao, Y. Li, Y. Ying, Electrochemical Conversion of Fe_3O_4 Magnetic Nanoparticles to Electroactive Prussian Blue Analogues for Self-Sacrificial Label Biosensing of Avian Influenza Virus H5N1, Anal. Chem. 89 (22) (2017) 12145–12151, https://doi.org/10.1021/acs.analchem.7b0278410.1021/acs.analchem.7b02784.s001.
[21] J. Prakash, J.C. Pivin, H.C. Swart, Noble metal nanoparticles embedding into polymeric materials: From fundamentals to applications, Adv. Colloid Interface Sci. 226 (Pt B) (2015) 187–202, https://doi.org/10.1016/j.cis.2015.10.010.
[22] T.K. Sau, A.L. Rogach, F. Jäckel, T.A. Klar, J. Feldmann, Properties and Applications of Colloidal Nonspherical Noble Metal Nanoparticles, Adv. Mater. 22 (16) (2010) 1805–1825, https://doi.org/10.1002/adma.200902557.
[23] L. Wang, R. Yan, Z. Huo, L. Wang, J. Zeng, J. Bao, X. Wang, Q. Peng, Y. Li, Fluorescence resonant energy transfer biosensor based on upconversion-luminescent nanoparticles, Angew. Chem. Int. Ed. 44 (37) (2005) 6054–6057, https://doi.org/10.1002/anie.200501907.
[24] E.S. Barrett, T.J. Dale, J. Rebek, Assembly and Exchange of Resorcinarene Capsules Monitored by Fluorescence Resonance Energy Transfer, J. Am. Chem. Soc. 129 (13) (2007) 3818–3819, https://doi.org/10.1021/ja070095610.1021/ja0700956.s001.
[25] H.-J. Lu, J.-J. Xu, H. Zhou, H.-Y. Chen, Recent advances in electrochemiluminescence resonance energy transfer for bioanalysis: Fundamentals and applications, Trends Anal. Chem. 122 (2020) 115746, https://doi.org/10.1016/j.trac.2019.115746.
[26] Y. Wang, D. Chao, Z. Wang, J. Ni, L. Li, An Energetic CuS–Cu Battery System Based on CuS Nanosheet Arrays, ACS Nano 15 (3) (2021) 5420–5427, https://doi.org/10.1021/acsnano.1c0007510.1021/acsnano.1c00075.s001.
[27] S. Adhikari, D. Sarkar, G. Madras, Hierarchical Design of CuS Architectures for Visible Light Photocatalysis of 4-Chlorophenol, ACS Omega 2 (7) (2017) 4009–4021, https://doi.org/10.1021/acsomega.7b00669.
[28] A. Curcio, A.V. de Walle, E. Benassai, A. Serrano, N. Luciani, N. Menguy, B. B. Manshian, A. Sargsian, S. Soenen, A. Espinosa, A. Abou-Hassan, C. Wilhelm, Massive Intracellular Remodeling of CuS Nanomaterials Produces Nontoxic Bioengineered Structures with Preserved Photothermal Potential, ACS Nano 15 (6) (2021) 9782–9795, https://doi.org/10.1021/acsnano.1c0056710.1021/acsnano.1c00567.s001.
[29] X. Li, P. Lu, B. Wu, Y. Wang, H. Wang, B. Du, X. Pang, Q. Wei, Electrochemiluminescence quenching of luminol by CuS in situ grown on reduced graphene oxide for detection of N-terminal pro-brain natriuretic peptide, Biosens. Bioelectron. 112 (2018) 40–47, https://doi.org/10.1016/j.bios.2018.04.030.
[30] J. Bath, A.J. Turberfield, DNA nanomachines, Nat. Nanotechnol. 2 (5) (2007) 275–284, https://doi.org/10.1038/nnano.2007.104.
[31] J.-S. Shin, N.A. Pierce, A Synthetic DNA Walker for Molecular Transport, J. Am. Chem. Soc. 126 (35) (2004) 10834–10835, https://doi.org/10.1021/ja047543j10.1021/ja047543j.s001.
[32] M. von Delius, D.A. Leigh, Walking molecules, Chem. Soc. Rev. 40 (7) (2011) 3656–3676, https://doi.org/10.1039/C1CS15005G.
[33] C. Feng, C. Zhang, J. Guo, G. Li, B. Ye, L. Zou, Novel preparation method of bipedal DNA walker based on hybridization chain reaction for ultrasensitive DNA biosensing, Anal. Chim. Acta 1176 (2021) 338781, https://doi.org/10.1016/j.aca.2021.338781.
[34] R. Yang, G. Jiang, H. Liu, L. He, F. Yu, Li'e Liu, L. Qu, Y. Wu, A dual-model "on-super off" photoelectrochemical/ratiometric electrochemical biosensor for ultrasensitive and accurate detection of microRNA-224, Biosens. Bioelectron. 188 (2021) 113337, https://doi.org/10.1016/j.bios.2021.113337.
[35] X. Cheng, Y. Bao, S. Liang, B.o. Li, Y. Liu, H. Wu, X. Ma, Y. Chu, Y. Shao, Q.i. Meng, G. Zhou, Q. Song, B. Zou, Flap Endonuclease 1-Assisted DNA Walkers for Sensitively and Specifically Sensing ctDNAs, Anal. Chem. 93 (27) (2021) 9593–9601, https://doi.org/10.1021/acs.analchem.1c0176510.1021/acs.analchem.1c01765.s001.
[36] N.a. Wu, K. Wang, Y.-T. Wang, M.-L. Chen, X.-W. Chen, T. Yang, J.-H. Wang, Three-Dimensional DNA Nanomachine Biosensor by Integrating DNA Walker and Rolling Machine Cascade Amplification for Ultrasensitive Detection of Cancer-Related Gene, Anal. Chem. 92 (16) (2020) 11111–11118, https://doi.org/10.1021/acs.analchem.0c0107410.1021/acs.analchem.0c01074.s001.
[37] S.D. Mason, Y. Tang, Y. Li, X. Xie, F. Li, Emerging bioanalytical applications of DNA walkers, Trends Anal. Chem. 107 (2018) 212–221, https://doi.org/10.1016/j.trac.2018.08.015.
[38] D.Y. Zhang, E. Winfree, Control of DNA Strand Displacement Kinetics Using Toehold Exchange, J. Am. Chem. Soc. 131 (47) (2009) 17303–17314, https://doi.org/10.1021/ja906987s.
[39] X. Qu, D. Zhu, G. Yao, S. Su, J. Chao, H. Liu, X. Zuo, L. Wang, J. Shi, L. Wang, W. Huang, H. Pei, C. Fan, An Exonuclease III-Powered, On-Particle Stochastic DNA Walker, Angew. Chem. Int. Ed. 56 (7) (2017) 1855–1858, https://doi.org/10.1002/anie.201611777.
[40] J. Nai, Y. Lu, L.e. Yu, X. Wang, X.W.D. Lou, Formation of Ni-Fe Mixed Diselenide Nanocages as a Superior Oxygen Evolution Electrocatalyst, Adv. Mater. 29 (41) (2017) 1703870, https://doi.org/10.1002/adma.201703870.
[41] X. Deng, K. Li, X. Cai, B. Liu, Y.i. Wei, K. Deng, Z. Xie, Z. Wu, P. Ma, Z. Hou, Z. Cheng, J. Lin, A Hollow-Structured CuS@Cu_2S@Au Nanohybrid: Synergistically Enhanced Photothermal Efficiency and Photoswitchable Targeting Effect for Cancer Theranostics, Adv. Mater. 29 (36) (2017) 1701266, https://doi.org/10.1002/adma.201701266.
[42] H. Cheng, C.-Y. Su, Z.-Y. Tan, S.-Z. Tai, Z.-Q. Liu, Interacting $ZnCo_2O_4$ and Au nanodots on carbon nanotubes as highly efficient water oxidation electrocatalyst, J. Power Sources 357 (2017) 1–10, https://doi.org/10.1016/j.jpowsour.2017.04.091.
[43] H. Liang, J. Lin, H. Jia, S. Chen, J. Qi, J. Cao, T. Lin, W. Fei, J. Feng, Hierarchical NiCo-LDH@NiOOH core-shell heterostructure on carbon fiber cloth as battery-like electrode for supercapacitor, J. Power Sources 378 (2018) 248–254, https://doi.org/10.1016/j.jpowsour.2017.12.046.
[44] J. Lin, Y. Liu, Y. Wang, H. Jia, S. Chen, J. Qi, C. Qu, J. Cao, W. Fei, J. Feng, Rational construction of nickel cobalt sulfide nanoflakes on CoO nanosheets with the help of carbon layer as the battery-like electrode for supercapacitors, J. Power Sources 362 (2017) 64–72, https://doi.org/10.1016/j.jpowsour.2017.07.014.
[45] X.-Y. Yu, Y.i. Feng, Y. Jeon, B. Guan, X.W.D. Lou, U. Paik, Formation of Ni-Co-MoS_2 Nanoboxes with Enhanced Electrocatalytic Activity for Hydrogen Evolution, Adv. Mater. 28 (40) (2016) 9006–9011, https://doi.org/10.1002/adma.201601188.
[46] M. Hu, H. Tian, J. He, Unprecedented Selectivity and Rapid Uptake of CuS Nanostructures toward Hg(II) Ions, ACS Appl. Mater. Interfaces 11 (21) (2019) 19200–19206, https://doi.org/10.1021/acsami.9b0464110.1021/acsami.9b04641.s001.
[47] N. Zhu, A. Zhang, Q. Wang, P. He, Y. Fang, Electrochemical detection of DNA hybridization using methylene blue and electro-deposited zirconia thin films on gold electrodes, Anal. Chim. Acta 510 (2) (2004) 163–168, https://doi.org/10.1016/j.aca.2004.01.017.
[48] R.K. Shervedani, S. Pourbeyram, A modification free hybridization biosensor for detection of DNA sequence based on Zr(IV) ion glue mediated the adsorption on Au–MPA SAM electrode, Sens. Actuators B Chem. 160 (1) (2011) 145–153, https://doi.org/10.1016/j.snb.2011.07.025.
[49] K.-J. Feng, Y.-H. Yang, Z.-J. Wang, J.-H. Jiang, G.-L. Shen, R.-Q. Yu, A nano-porous CeO_2/Chitosan composite film as the immobilization matrix for colorectal cancer DNA sequence-selective electrochemical biosensor, Talanta 70 (3) (2006) 561–565, https://doi.org/10.1016/j.talanta.2006.01.009.
[50] P. Teengam, W. Siangproh, A. Tuantranont, T. Vilaivan, O. Chailapakul, C. S. Henry, Electrochemical impedance-based DNA sensor using pyrrolidinyl peptide nucleic acids for tuberculosis detection, Anal. Chim. Acta 1044 (2018) 102–109, https://doi.org/10.1016/j.aca.2018.07.045.
[51] G.-J. Li, L.-H. Liu, X.-W. Qi, Y.-Q. Guo, W. Sun, X.-L. Li, Development of a sensitive electrochemical DNA sensor by 4-aminothiophenol self-assembled on electrodeposited nanogold electrode coupled with Au nanoparticles labeled reporter ssDNA, Electrochim. Acta 63 (2012) 312–317, https://doi.org/10.1016/j.electacta.2011.12.107.